# NUMERICAL SIMULATION OF NAPL VAPOR TRANSPORT IN AIR[*]

ONDŘEJ PÁRTL [†], MICHAL BENEŠ [‡], AND PETER FROLKOVIČ [§]

**Abstract.** We present a mathematical and numerical model for non-isothermal, compressible flow of a mixture of two ideal gases subject to gravity. The mathematical model is based on balance equations for mass, momentum and energy combined with the ideal gas equation of state. The numerical model is based on the method of lines; the spatial discretization is carried out by means of the control volume based finite element method, and for the time integration, the Runge-Kutta-Merson method is used. Finally, we present preliminary results of numerical experiments that illustrate the ability of our numerical scheme.

**Key words.** control volume based finite element method, multicomponent flow, compressible flow

**AMS subject classifications.** 76M10, 76M12, 76R99, 35Q35

**1. Introduction.** In our research, we develop a numerical model for simulation of NAPL (Non-Aqueous Phase Liquids) vapor transport driven by air flow in porous medium and above its surface. The goal of this research is to put together a mathematical model for these phenomena, and to implement a numerical solver in which these flows are solved separately, and the information is passed between the flows via coupling conditions on the interface between the media (similarly as in [1]). Such a numerical model can be used, for example, for modeling the intrusion of NAPL vapor into buildings from contaminated soil [5].

To the best of our knowledge, researches in the area of free flow concentrate on incompressible flows (e.g., [1], [9]) or compressible flows without gravity effects, where the interaction of the species in the mixture is differently detailed (e.g., [10], [7]). In this contribution, we present the part of our model of the coupled flows that describes the free flow. This model is based on the kinetic theory of gas mixtures [3], [4], [6], and it includes the gravity effects as well.

We also present preliminary results of numerical tests that demonstrate the ability of our model.

**2. Mathematical Model.** According to the theory described in [3], [4], [6], a mixture of two polyatomic ideal gases (the first one will be referred to as 'gas' and the second one as 'NAPL vapor') can be described by the following conservation laws:

- Conservation equation for the mass of the mixture

$$(2.1) \qquad \frac{\partial \rho}{\partial t} + \nabla \cdot (\rho \boldsymbol{v}) = 0.$$

- Conservation equation for the mass of the NAPL vapor

$$(2.2) \qquad \frac{\partial \rho_n}{\partial t} + \nabla \cdot [\rho_n (\boldsymbol{v} + \boldsymbol{V_n})] = 0.$$

- Conservation equation for the momentum of the mixture

$$(2.3) \qquad \frac{\partial (\rho \boldsymbol{v})}{\partial t} + \nabla \cdot (\boldsymbol{P} + \rho \boldsymbol{v} \otimes \boldsymbol{v}) = \rho \boldsymbol{g}.$$

- Conservation equation for the energy of the mixture

$$(2.4) \qquad \frac{\partial (\rho e)}{\partial t} + \nabla \cdot (\boldsymbol{Q} + \rho e \boldsymbol{v} + \boldsymbol{P} \cdot \boldsymbol{v}) = \rho \boldsymbol{g} \cdot \boldsymbol{v}.$$

In these equations, the quantities without subscripts refer to the whole mixture; the quantities related to the NAPL vapor and gas are denoted by the subscript $n$ and $g$, respectively. Vectors and matrices are printed in the bold font, and their components are in the non-bold font, i.e., $\boldsymbol{v} = (v_1, v_2)^T$, where $T$ denotes the transposition. $\rho$ [kg $\cdot$ m$^{-3}$] represents the density, $t$ [s] the time, $\boldsymbol{v}$ [m $\cdot$ s$^{-1}$] the velocity, $\rho_i$ [kg $\cdot$ m$^{-3}$] the partial density of the component $i$ ($\sum_{i \in \{n,g\}} \rho_i = \rho$), $\boldsymbol{V}_i$ [m $\cdot$ s$^{-1}$] the diffusion velocity of the component $i$, $\boldsymbol{P}$ [Pa] the pressure tensor and $\boldsymbol{g}$ [m$\cdot$s$^{-2}$] the gravitational acceleration vector. The symbol $\otimes$ stands for the tensor product. $e$ [m$^2 \cdot$ s$^{-2}$] is the specific energy and $\boldsymbol{Q}$ [kg $\cdot$ s$^{-3}$] the heat flow vector. The fluxes $\boldsymbol{V}_i$, $\boldsymbol{P}$ and $\boldsymbol{Q}$ are defined as

$$(2.5) \qquad \boldsymbol{V}_i = - \sum_{j \in \{n,g\}} D_{i,j} (\boldsymbol{d}_j + k_{Tj} \nabla \ln T), \ i = g, n,$$

$$(2.6) \qquad \boldsymbol{P} = p\boldsymbol{I} - 2\mu\boldsymbol{S},$$

$$(2.7) \qquad \boldsymbol{Q} = -\lambda \nabla T + p \sum_{i \in \{n,g\}} \left(k_{Ti} + \frac{\kappa}{\kappa - 1} \frac{p_i}{p}\right) \boldsymbol{V_i},$$

where $\boldsymbol{d}_i$ [m$^{-1}$] is the diffusion driving force defined by

$$(2.8) \qquad \boldsymbol{d}_i = \nabla \left(\frac{p_i}{p}\right) + \left(\frac{p_i}{p} - X_i\right) \nabla \ln p,$$

where $p_i$ [Pa] and $X_i$ [$-$] are the partial pressure and mass fraction of the component $i$ ($\sum_{i \in \{n,g\}} p_i = p$, $\sum_{i \in \{n,g\}} X_i = 1$), respectively, and $p$ [Pa] is the pressure. $D_{i,j}$ [m$^2 \cdot$ s$^{-1}$] is the multicomponent diffusion coefficient, $D_{i,j} = D_{j,i}$ and $D_{i,i} = -\frac{\rho_j}{\rho_i} D_{j,i}$ if $\rho_i \neq 0$; otherwise, $D_{i,i}$ is not needed. $k_{Ti}$ [$-$] denotes the thermal diffusion ratio, $k_{Tn} = -k_{Tg}$, $\mu$ [kg$\cdot$m$^{-1}\cdot$s$^{-1}$] is the dynamic viscosity, $\boldsymbol{S}$ [s$^{-1}$] the rate-of-shear tensor defined by

$$(2.9) \qquad \boldsymbol{S}_{i,j} = \frac{1}{2} \left(\frac{\partial v_j}{\partial x_i} + \frac{\partial v_i}{\partial x_j}\right) - \frac{1}{3} \nabla \cdot \boldsymbol{v} \delta_{i,j},$$

where $x_i$ [m], $i = 1, 2$, are spatial coordinates, and $\delta_{i,j}$ is the Kronecker delta. $\lambda$ [kg·m·K$^{-1}$·s$^{-3}$] denotes the thermal conductivity coefficient, $T$ [K] the thermodynamic temperature and $\kappa = \frac{c_p}{c_v}$ [−] the ratio of specific heats, where $c_p$ [J·kg$^{-1}$·K$^{-1}$] and $c_V$ [J·kg$^{-1}$·K$^{-1}$] denote the specific heat at constant pressure and volume, respectively.

The previous system is supplemented by the following formula relating the energy to the temperature

$$(2.10) \qquad \rho e = c_V \rho T + \frac{1}{2}\rho \boldsymbol{v}^2$$

and by the ideal gas equation of state

$$(2.11) \qquad \rho = p\frac{\overline{M}}{RT},$$

where $R$ [J · K$^{-1}$ · mol$^{-1}$] denotes the gas constant, and $\overline{M}$ [kg · mol$^{-1}$] is the molar mass defined by

$$(2.12) \qquad \overline{M} = \left( \sum_{i \in \{n,g\}} \frac{X_i}{M_i} \right)^{-1},$$

where $M_i$ [kg · mol$^{-1}$] is the molar mass of the component $i$. Combining equations (2.10) and (2.11) with the Mayer relation $\overline{M}(c_p - c_V) = R$, we get the formula relating the energy to the pressure

$$(2.13) \qquad p = (\kappa - 1) \left( \rho e - \frac{1}{2}\boldsymbol{v}^2 \rho \right).$$

Note that for $\rho_n = 0$, the governing equations reduce to the compressible Navier-Stokes equations and the corresponding energy balance equation.

The equations are solved in a rectangular domain $\Omega \subset \mathbb{R}^2$ and on a time interval $[t_{\text{ini}}, t_{\text{fin}}]$. The initial conditions are

$$(2.14) \qquad \rho(t_{\text{ini}}, \boldsymbol{x}) = \rho_{\text{ini}}(\boldsymbol{x}), \qquad \rho_n(t_{\text{ini}}, \boldsymbol{x}) = \rho_{n,\text{ini}}(\boldsymbol{x}),$$
$$(2.15) \qquad T(t_{\text{ini}}, \boldsymbol{x}) = T_{\text{ini}}(\boldsymbol{x}), \qquad \boldsymbol{v}(t_{\text{ini}}, \boldsymbol{x}) = \boldsymbol{v}_{\text{ini}}(\boldsymbol{x})$$

for $\boldsymbol{x} \in \overline{\Omega}$. The boundary conditions will be discussed later on.

**3. Numerical Solution.** The aforementioned mathematical problem is solved by means of the method of lines, where the spatial discretization is carried out by the control volume based finite element method [12]. For the time integration, the Runge-Kutta-Merson method [11] is employed.

All of the unknown functions (the products $\rho v_i$, $i = g, n$, and $\rho e$ are treated as a single variable) are approximated using the classical finite element space based on the bilinear Lagrange rectangles [11], where the domain $\Omega$ is covered by a mesh $\mathcal{T} = \{T^e\}_{e=1}^{N_{\mathcal{T}}}$ of rectangles (see Figure 3.1), where $N_{\mathcal{T}}$ stands for the number of rectangles in $\mathcal{T}$. Each vertex $\boldsymbol{x}_i$ of the mesh is associated with the basis function $\varphi_i$. Further, we use the node-centered dual mesh of finite volumes $\mathcal{V} = \{V_i\}_{i=1}^{N_{\mathcal{V}}}$, where $N_{\mathcal{V}}$ denotes the number of nodes in $\mathcal{T}$. This mesh will be described later on.

The following notation will be used throughout this text:
  • $\mathcal{X} = \{\boldsymbol{x}_i\}_{i=1}^{N_{\mathcal{V}}}$ is the set of all vertices in the mesh $\mathcal{T}$;
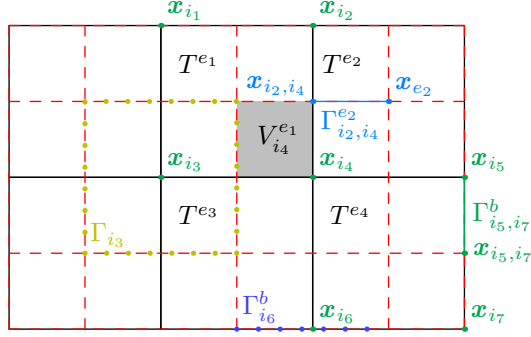
Fig. 3.1: Mesh of rectangles (solid line) and dual mesh (dashed line). According to the notation introduced in Section 3, we have $\Lambda^{e_1} = \{i_1, i_2, i_3, i_4\}$, $\Lambda_{i_4} = \{i_2, i_3, i_5, i_6\}$, $\Lambda_{i_4}^{e_1} = \{i_2, i_3\}$, $\Lambda_{i_4}^b = \{i_2, i_5, i_6\}$, $\Lambda_{i_2,i_4} = \{e_1, e_2\}$ and $\Lambda_{i_4}^n = \{e_1, e_2, e_3, e_4\}$. The gray region is $V_{i_4}^{e_1}$.

- $\Lambda^e = \{i | \boldsymbol{x}_i \in T^e\}$;
- $\Lambda_i$ is the set of all indices $j$ different from $i$ for which the line segment connecting the nodes $\boldsymbol{x}_i$ and $\boldsymbol{x}_j$ is an edge of a rectangle in $\mathcal{T}$;
- $\Lambda_i^e = \Lambda^e \cap \Lambda_i$;
- $\Lambda_i^b = \Lambda_i \cap \{j | \boldsymbol{x}_j \in \partial\Omega\}$;
- $\Lambda_{i,j} = \{e | i \in \Lambda^e \wedge j \in \Lambda^e\}$;
- $\Lambda_i^n = \{e | i \in \Lambda^e\}$;
- $\boldsymbol{x}_{i,j}$ is the midpoint of the line segment connecting the vertices $\boldsymbol{x}_i$ and $\boldsymbol{x}_j$;
- $\boldsymbol{x}_e$ is the circumcenter of $T^e$;
- $\Gamma_{i,j}^e$ is the line segment connecting the points $\boldsymbol{x}_e$ and $\boldsymbol{x}_{i,j}$;
- $\Gamma_{i,j}^b$ is the line segment connecting the boundary points $\boldsymbol{x}_i$ and $\boldsymbol{x}_{i,j}$;
- $\Gamma_i = \bigcup_{j \in \Lambda_i} \bigcup_{e \in \Lambda_{i,j}} \Gamma_{i,j}^e$;
- $\Gamma_i^b = \bigcup_{j \in \Lambda_i^b} \Gamma_{i,j}^b$ for $\boldsymbol{x}_i \in \partial\Omega$;
- $\boldsymbol{x}_{i,j}^e$ and $\boldsymbol{x}_{i,j}^b$ are the midpoints of $\Gamma_{i,j}^e$ and $\Gamma_{i,j}^b$, respectively;
- $V_i^e = V_i \cap T^e$;
- $f(\boldsymbol{x}_i) = f_i$, $f(\boldsymbol{x}_{i,j}) = f_{i,j}$, $f(\boldsymbol{x}_{i,j}^e) = f_{i,j}^e$, $f(\boldsymbol{x}_{i,j}^b) = f_{i,j}^b$, $f(\boldsymbol{x}_e) = f_e$, where the time coordinate is omitted;
- $[\boldsymbol{f}]_k$ denotes the $k$-th component of the vector $\boldsymbol{f}$, when there are too many symbols in the definition of $\boldsymbol{f}$.

The preceding notation will be used for scalar ($f$) as well as vector-valued ($\boldsymbol{f}$) functions.

The finite volume $V_i$ associated with the node $\boldsymbol{x}_i$ is defined as the open set surrounded by the piecewise linear curve $\Gamma_i$ (i.e., $\partial V_i = \Gamma_i$) for $\boldsymbol{x}_i \notin \partial\Omega$ and by the piecewise linear curve $\Gamma_i \cup \Gamma_i^b$ (i.e., $\partial V_i = \Gamma_i \cup \Gamma_i^b$) for $\boldsymbol{x}_i \in \partial\Omega$. The dual mesh of finite volumes is depicted in Figure 3.1.

In our computations, the physical domain $\Omega$ is extended by one layer of dummy elements [2], and the boundary conditions are prescribed at the corresponding dummy nodes. Therefore, equations (2.1)–(2.4) are solved in the whole of $\Omega$.

The numerical scheme is derived by integrating equations (2.1)–(2.4) over a volume $V_i$, applying the Green formula and using the following approximation formulas:

- $\int_{V_i} f(\boldsymbol{x}) \, d\boldsymbol{x} \doteq \sum_{e \in \Lambda_i^n} |V_i^e| f_i = |V_i| f_i$, where $|V_i^e|$ denotes the area of $V_i^e$.

- $\int_{V_i} (\nabla f)(\boldsymbol{x}) \, \mathrm{d}\boldsymbol{x} \doteq \sum_{e \in \Lambda_i^n} |V_i^e| (\nabla f)_e$.
- $\int_{\Gamma_i} \boldsymbol{f}(\boldsymbol{x}) \cdot \boldsymbol{n} \, \mathrm{d}\boldsymbol{x} \doteq \sum_{j \in \Lambda_i} \sum_{e \in \Lambda_{i,j}^e} \left| \Gamma_{i,j}^e \right| \boldsymbol{f}_{i,j}^e \cdot \boldsymbol{n}_{i,j}^e$, where $\left| \Gamma_{i,j}^e \right|$ denotes the length of the line segment $\Gamma_{i,j}^e$, and $\boldsymbol{n}_{i,j}^e$ is the unit outward normal with respect to $\Gamma_{i,j}^e$.

The previous procedure yields the system of ordinary differential equations for $k = 1, 2$ and $i = 1, 2, \ldots N_{\mathcal{V}}$ (the dummy nodes are used),

$$(3.1) \qquad \sum_{e \in \Lambda_i^n} |V_i^e| \dot{\rho}_i + \sum_{j \in \Lambda_i} \sum_{e \in \Lambda_{i,j}} \left| \Gamma_{i,j}^e \right| \underline{\rho_{i,j}^e \boldsymbol{v}_{i,j}^e} \cdot \boldsymbol{n}_{i,j}^e = 0,$$

$$(3.2) \qquad \sum_{e \in \Lambda_i^n} |V_i^e| \dot{\rho}_{n,i} + \sum_{j \in \Lambda_i} \sum_{e \in \Lambda_{i,j}} \left| \Gamma_{i,j}^e \right| \underline{\rho_{n,i,j}^e} \left( \boldsymbol{v}_{i,j}^e + \boldsymbol{V}_{n,i,j}^e \right) \cdot \boldsymbol{n}_{i,j}^e = 0,$$

$$
(3.3) \qquad
\begin{aligned}
\sum_{e \in \Lambda_i^n} |V_i^e| (\dot{\rho v_k})_i &+ \sum_{e \in \Lambda_i^n} |V_i^e| [(\nabla p)_e]_k + \sum_{j \in \Lambda_i} \sum_{e \in \Lambda_{i,j}} \left| \Gamma_{i,j}^e \right| \left[ (\boldsymbol{P} - p\boldsymbol{I})_{i,j}^e \cdot \boldsymbol{n}_{i,j}^e \right]_k \\
&+ \sum_{j \in \Lambda_i} \sum_{e \in \Lambda_{i,j}} \left| \Gamma_{i,j}^e \right| \underline{(\rho v_k)_{i,j}^e} \boldsymbol{v}_{i,j}^e \cdot \boldsymbol{n}_{i,j}^e = \sum_{e \in \Lambda_i^n} |V_i^e| \rho_i g_k,
\end{aligned}
$$

$$
(3.4) \qquad
\begin{aligned}
\sum_{e \in \Lambda_i^n} |V_i^e| (\dot{\rho e})_i &+ \sum_{j \in \Lambda_i} \sum_{e \in \Lambda_{i,j}} \left| \Gamma_{i,j}^e \right| \left[ (\boldsymbol{P} \cdot \boldsymbol{v})_{i,j}^e + \boldsymbol{Q}_{i,j}^e + \underline{(\rho e)_{i,j}^e \boldsymbol{v}_{i,j}^e} \right] \cdot \boldsymbol{n}_{i,j}^e \\
&= \sum_{e \in \Lambda_i^n} |V_i^e| \boldsymbol{g} \cdot (\rho \boldsymbol{v})_i,
\end{aligned}
$$

where

$$(3.5) \qquad \boldsymbol{V}_{n,i,j}^e = - \sum_{l \in \{n,g\}} D_{n,l,i,j}^e \left( \boldsymbol{d}_{l,i,j}^e + k_{T_l,i,j}^e \frac{\nabla T_{i,j}^e}{T_{i,j}^e} \right),$$

$$(3.6) \qquad \boldsymbol{d}_{l,i,j}^e = \nabla \left( \frac{p_l}{p} \right)_{i,j}^e + \left( \frac{p_{l,i,j}^e}{p_{i,j}^e} - X_{l,i,j}^e \right) \frac{\nabla p_{i,j}^e}{p_{i,j}^e},$$

$$(3.7) \qquad \boldsymbol{P}_{i,j}^e = (p\boldsymbol{I} - 2\mu\boldsymbol{S})_{i,j}^e,$$

$$(3.8) \qquad \boldsymbol{Q}_{i,j}^e = -\lambda (\nabla T)_{i,j}^e + p_{i,j}^e \sum_{l \in \{n,g\}} \left( k_{T_l,i,j}^e + \frac{\kappa}{\kappa - 1} \left( \frac{p_{l,i,j}^e}{p_{i,j}^e} \right) \right) \boldsymbol{V}_{l,i,j}^e.$$

For stability reasons, the term $\int_{V_i} \nabla p$ is approximated as the volume integral in (3.3), and the underlined terms are modified by the full upwind formula

$$
f_{i,j}^e = \begin{cases} f_i, & \boldsymbol{v}_{i,j}^e \cdot \boldsymbol{n}_{i,j}^e \geq 0 \\ f_j, & \boldsymbol{v}_{i,j}^e \cdot \boldsymbol{n}_{i,j}^e < 0 \end{cases} .
$$

The terms $\nabla v_k$ and $\nabla \left( \frac{p_k}{p} \right)$ are calculated via

$$\nabla v_k = \nabla \left( \frac{(\rho v_k)}{\rho} \right) = \frac{\rho \nabla (\rho v_k) - (\rho v_k) \nabla \rho}{\rho^2}, \quad \nabla \left( \frac{p_k}{p} \right) = \frac{p \nabla p_k - p_k \nabla p}{p^2}.$$

Similarly, the terms $\nabla \ln T$ and $\nabla \ln p$ are replaced by $\frac{\nabla T}{T}$ and $\frac{\nabla p}{p}$, respectively, in (3.5) and (3.6).

| par. | value | unit | par. | value | unit |
|---|---|---|---|---|---|
| $D_{g,n}$ | $-8.35 \cdot 10^{-5}$ | $\text{m}^2 \cdot \text{s}^{-1}$ | $g_1$ | 0.0 | $\text{m} \cdot \text{s}^{-2}$ |
| $\mu$ | $1.725 \cdot 10^{-5}$ | $\text{kg} \cdot \text{m}^{-1} \cdot \text{s}^{-1}$ | $g_2$ | $-9.81$ | $\text{m} \cdot \text{s}^{-2}$ |
| $\lambda$ | 0.02428 | $\text{kg} \cdot \text{m} \cdot \text{K}^{-1} \cdot \text{s}^{-3}$ | $p_{\text{ref}}$ | 101325 | Pa |
| $\kappa$ | 1.4 | $-$ | $T_{\text{ref},1}$ | 295.15 | K |
| $M_{\text{g}}$ | 0.02896 | $\text{kg} \cdot \text{mol}^{-1}$ | $T_{\text{ref},2}$ | 294.65 | K |
| $M_{\text{n}}$ | 0.13139 | $\text{kg} \cdot \text{mol}^{-1}$ | $v_{\text{ref},1}$ | 1.0 | $\text{m} \cdot \text{s}^{-1}$ |
| $R$ | 8.3144621 | $\text{J} \cdot \text{K}^{-1} \cdot \text{mol}^{-1}$ | $v_{\text{ref},2}$ | 0.0 | $\text{m} \cdot \text{s}^{-1}$ |
| $X_{n,\text{ref}}$ | 0.001 | $-$ | | | |

Table 4.1: Values of constant physical parameters.

**4. Numerical Results.** In this section, results of two of our numerical tests are presented. Describing the boundary conditions, we shall use the abbreviations *lef*, *rig*, *top*, *bot* which refer to the left, right, top and bottom edge of $\Omega$.

**4.1. Spreading Wave of NAPL Vapor.** In this test, the domain $\Omega = (0.0, 3.0) \times (-0.5, 0.5)$ is considered, where the units are [m], and there are 120 and 40 square elements in the $x_1$- and $x_2$-direction, respectively. The same squares are used as the dummy elements. The following hydrostatic initial ($t_{\text{ini}} = 0.0$s) conditions are considered:

$$\rho_{\text{ini}}(\boldsymbol{x}) = p_{\text{ref}} \frac{M_g}{RT_{\text{ref},1}} \exp\left( \frac{M_g g_2}{RT_{\text{ref},1}} x_2 \right), \ \rho_{n,\text{ini}}(\boldsymbol{x}) = 0, \ T_{\text{ini}}(\boldsymbol{x}) = T_{\text{ref},1}, \ \boldsymbol{v}_{\text{ini}}(\boldsymbol{x}) = \boldsymbol{v}_{\text{ref}}.$$

At the dummy nodes, the following setup for $\boldsymbol{v}$, $\rho$, $\rho_n$ and $p$ is used:

- Left edge. $\boldsymbol{v}|_{\text{lef}}(\boldsymbol{x}) = \boldsymbol{v}_{\text{ref}}$,

$$\rho|_{\text{lef}}(\boldsymbol{x}) = (p_{\text{ref}} + 100.0) \frac{M_g}{RT_{\text{ref},1}} \exp\left( \frac{M_g g_2}{RT_{\text{ref},1}} x_2 \right), \ \rho_n|_{\text{lef}}(\boldsymbol{x}) = X_{n,\text{ref}}\rho|_{\text{lef}}(\boldsymbol{x});$$

  the pressure $p$ is extrapolated constantly.
- Right edge. $\boldsymbol{v}|_{\text{rig}}(\boldsymbol{x}) = \boldsymbol{v}_{\text{ref}}$; the densities $\rho$ and $\rho_n$ and the pressure $p$ are extrapolated constantly.
- Top and bottom edge. $\boldsymbol{v}|_{\text{top}}(\boldsymbol{x}) = \boldsymbol{v}_{\text{ref}}$, $\boldsymbol{v}|_{\text{bot}}(\boldsymbol{x}) = \boldsymbol{v}_{\text{ref}}$; the density $\rho_n$ is calculated from $X_n$, which is extrapolated constantly. The density $\rho$ and the pressure $p$ are extrapolated exponentially because for our $\boldsymbol{g}$, the hydrostatic pressure and density distribution at constant temperature is exponential. According to our experience, the exponential extrapolation of $p$ and $\rho$ together with the approximation of $\int_{V_i} \nabla p$ as a volume integral in (3.3) seems to be necessary if similar physical conditions are considered. Without these details, the scheme produces oscillations in the state variables which grow without limits.

The values of the physical constants are listed in Table 4.1. The coefficient $k_{Tn}$ is defined by the formula $k_{Tn} = 0.35 X_n \overline{M} M_n^{-1}$, which is based on information in [3].

The numerical results are presented in Figures 4.1–4.3. We can see how the wave of higher density and non-zero mass fraction of NAPL vapor spreads towards the right edge. As we need to model only slow flows with minor differences in the densities over very long time intervals in our application, the fact that the wavefront is smeared
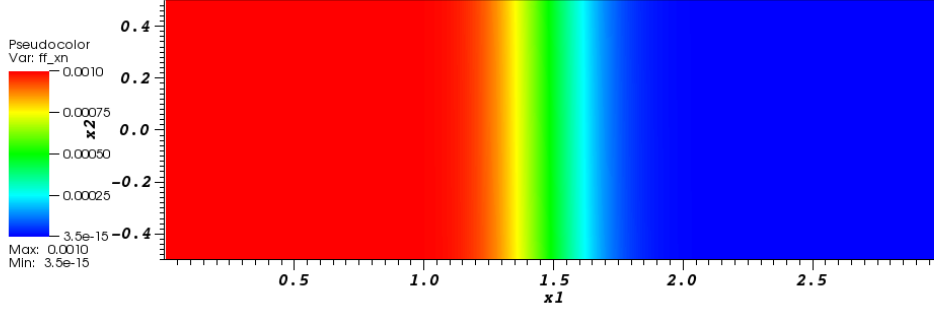
Fig. 4.1: Spreading wave of NAPL Vapor on mesh 120x40. Mass fraction of NAPL vapor $X_n$ $[-]$ at time $t = 1.5$s.
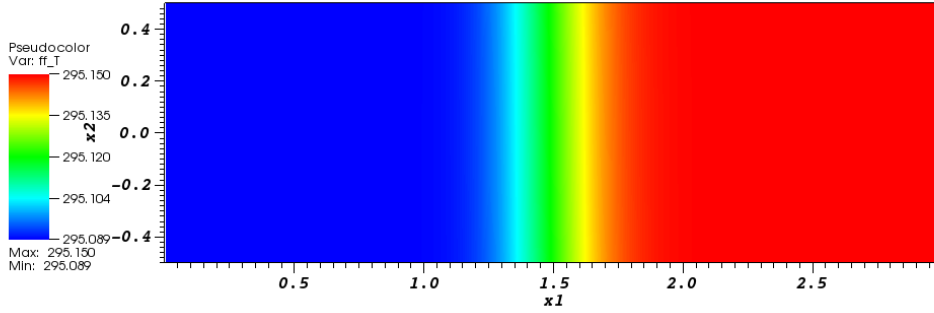


Fig. 4.2: Spreading wave of NAPL Vapor on mesh 120x40. Temperature $T$ [K] at time $t = 1.5$s.

should not pose any problems in our research. Note that the wavefront in 4.3 seems to be skew because the height of the density differs in the $x_2$-direction. The final density distribution equals to the density profile prescribed on the left edge at every $x_1 \in [0.0, 3.0]$.

Finally, Figure 4.4 shows the density distribution in the same test, where the spatial mesh has 480 and 160 elements in the $x_1$- and $x_2$-direction, respectively. Comparing Figures 4.3 and 4.4, it seems that the numerical solution converges.

**4.2. Natural Convection.** This test is motivated by the temperature induced air circulation in a well which is studied in [8]. We consider the domain $\Omega = (0.0, 0.1) \times (-0.05, 0.05)$, where the units are [m], and there are 10 and 10 square elements in the $x_1$- and $x_2$-direction, respectively. The same squares are used as the dummy elements. The following initial ($t_{\mathrm{ini}} = 0.0$s) conditions are considered:

$$T_{\mathrm{ini}}(\boldsymbol{x}) = T_{\mathrm{slo}}x_2 + T_{\mathrm{shi}}, \text{ where } T_{\mathrm{slo}} = \frac{T_{\mathrm{ref},2} - T_{\mathrm{ref},1}}{0.05 - (-0.05)} \text{ and } T_{\mathrm{shi}} = T_{\mathrm{ref},1} + 0.05 \cdot T_{\mathrm{slo}};$$

$$\rho_{n,\mathrm{ini}}(\boldsymbol{x}) = 0, \ \boldsymbol{v}_{\mathrm{ini}}(\boldsymbol{x}) = (0,0)^{\mathrm{T}}, \ \rho_{\mathrm{ini}}(\boldsymbol{x}) = p_{\mathrm{ref}}\frac{M_g}{RT_{\mathrm{ini}}(\boldsymbol{x})} \left(\frac{T_{\mathrm{ini}}(\boldsymbol{x})}{T_{\mathrm{ref},1}}\right)^{\frac{M_g g_2}{T_{\mathrm{slo}}R}}.$$

Note that the previous conditions are hydrostatic with the temperature $T$ decreasing from $T_{\mathrm{ref},1}$ to $T_{\mathrm{ref},2}$.
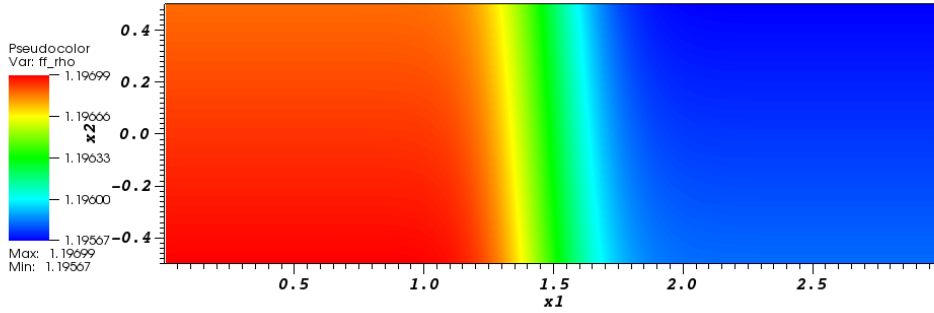
Fig. 4.3: Spreading wave of NAPL Vapor on mesh 120x40. Density $\rho$ [kg · m$^{-3}$] at time $t = 1.5$s.
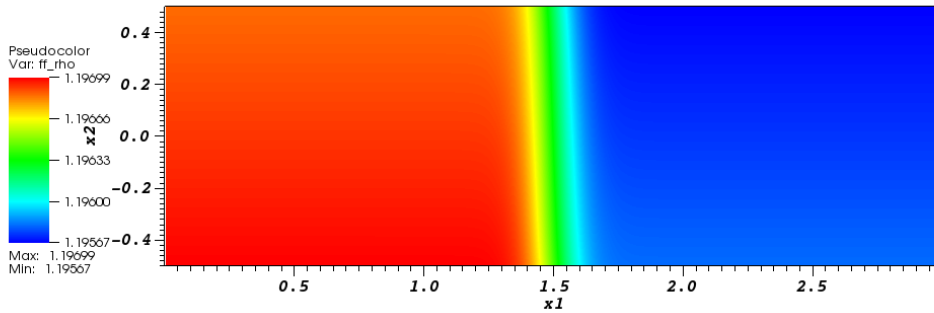


Fig. 4.4: Spreading wave of NAPL Vapor on mesh 480x160. Density $\rho$ [kg · m$^{-3}$] at time $t = 1.5$s.

At the dummy nodes, the following setup for $v$, $\rho$, $\rho_n$, $T$ and $p$ is used:

- Left and right edge. $v|_{\text{lef}}(x) = (0,0)^{\text{T}}$ and $v|_{\text{rig}}(x) = (0,0)^{\text{T}}$; the densities $\rho$ and $\rho_n$ and the pressure $p$ are extrapolated constantly.
- Top and bottom edge. $v|_{\text{top}}(x) = (0,0)^{\text{T}}$, $v|_{\text{bot}}(x) = (0,0)^{\text{T}}$; $T|_{\text{bot}}(x) = T_{\text{ref},1}$, $T|_{\text{top}}(x) = T_{\text{ref},2}$. The densities $\rho_n$ and $\rho$ are extrapolated constantly and linearly, respectively.

Note that we do not need any Dirichlet boundary conditions for $p$ or $\rho$.

The values of the physical constants are listed in Table 4.1. The coefficient $k_{Tn}$ is not needed.

The numerical results in a steady state are presented in Figures 4.5 and 4.6. We can see that two circulation cells appear. As we do not apply any numerical stabilization in our scheme, in accordance with [12], there are oscillations in the pressure $p$ in order of Pascals along the vertical axis of symmetry of the domain $\Omega$.

**5. Conclusions.** In this section, we want to discuss the aforementioned numerical results. The method which we use for the spatial discretization was chosen because it is simple, and it seems not to produce any non-physical oscillation in the density $\rho_n$ and mass fraction $X_n$. But it can produce oscillations in the pressure $p$, and it can add too much artificial diffusion in the regions where the gradient of the solution is discontinuous. The former can be prevented by using the staggered arrangement of the variables [12]. According to [1], an another option can be to add a stabilization
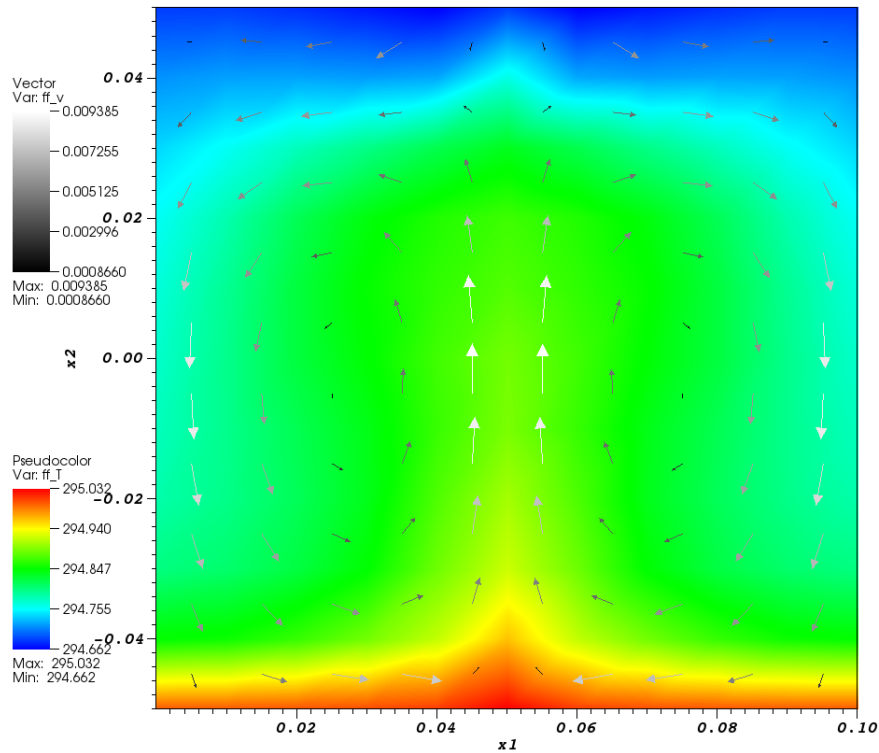
Fig. 4.5: Natural Convection. Temperature $T$ [K] at time $t = 900.0$s. The arrows indicate the direction and magnitude of the velocity $\boldsymbol{v}$ [m · s$^{-1}$].

term into equation (3.1). The tests of various stabilization terms are our next step in the development of the model. In our opinion, the later disadvantage should not pose any problems in our future research.

Finally, the approximation of the term $\int_{V_i} \nabla p$ in (3.3) as a volume integral together with the exponential extrapolation of $p$ and $\rho$ which we employ in the Section 4.1 seems to be necessary when modeling systems in which the hydrostatic distribution of $p$ and $\rho$ is exponential.

## REFERENCES

[1] K. BABER, K. MOSTHAF, B. FLEMISCH, R. HELMIG, S. MÜTHING, AND B. WOHLMUTH, *Numerical scheme for coupling two-phase compositional porous-media flow and one-phase compositional free flow*, IMA Journal of Applied Mathematics, 77 (2012), pp. 887–909.

[2] J. BLAZEK, *Computational Fluid Dynamics: Principles and Applications*, Elsevier Science, 2001.

[3] S. CHAPMAN AND T. G. COWLING, *The Mathematical Theory of Non-Uniform Gases*, Second ed., Cambridge University Press, 1952.

[4] J. H. FERZIGER AND H. G. KAPER, *Mathematical Theory of Transport Processes in Gases*, First ed., North-Holland Publishing Company, 1972.

[5] D. FOLKES, W. WERTZ, J. KURTZ AND T. KUEHSTER, *Observed Spatial and Temporal Distributions of CVOCs at Colorado and New York Vapor Intrusion Sites*, Ground Water Monitoring & Remediation, 29 (2009), pp. 70–80.
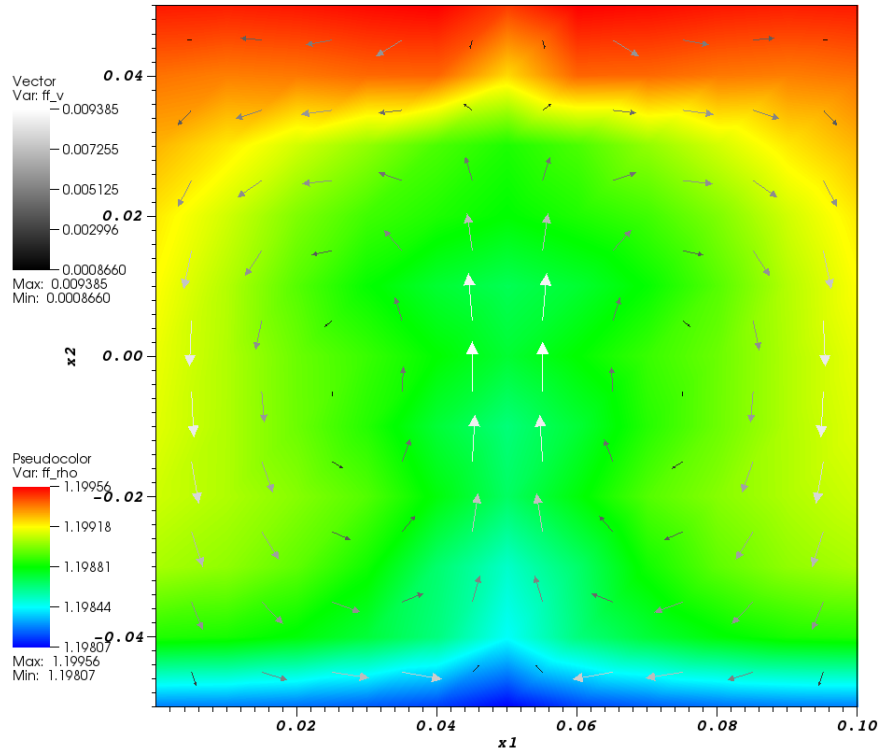
Fig. 4.6: Natural Convection. Density $\rho$ [kg $\cdot$ m$^{-3}$] at time $t = 900.0$s. The arrows indicate the direction and magnitude of the velocity $\boldsymbol{v}$ [m $\cdot$ s$^{-1}$].

[6]  V. Giovangigli, *Multicomponent Flow Modeling*, First ed., Birkhuser Boston, 1999.

[7]  H. Gómez, I. Colominas, F. Navarrina, and M. Casteleiro, *A mathematical model and a numerical model for hyperbolic mass transport in compressible flows*, Heat and Mass Transfer, 45 (2008), pp. 219–226.

[8]  J. Hovorka, R. F. Holub, V. Ždímal, J. Bendl and P. K. Hopke, *The mystery "Well": A natural cloud chamber?*, Journal of Aerosol Science, 81 (2015), pp. 70–74.

[9]  O. A. Neves, E. C. Romao, J. B. Campos-Silva, *Numeric simulation of pollutant dispersion by a control-volume based on finite element method*, International Journal for Numerical Methods in Fluids, 66 (2011), pp. 1073–1092.

[10]  R. Ouzani, M. Si-Ameur, *Numerical study of hydrogene–air mixing in turbulent compressible coaxial jets*, International Journal of Hydrogene Energy, 40 (2015), pp. 9539–9554.

[11]  O. Pártl, *Computational Studies of Bacterial Colony Model*, American Journal of Computational Mathematics, 3 (2013), pp. 147–157.

[12]  S. Patankar, *Numerical Heat Transfer and Fluid Flow*, Taylor & Francis, 1980.